

# The materials science X-ray beamline BL8 at the DELTA storage ring

Dirk Lützenkirchen-Hecht,\* Ralph Wagner, Ulrich Haake, Anke Watenphul‡ and Ronald Frahm

Fachbereich C - Physik, Bergische Universität Wuppertal, Gausstrasse 20, 42097 Wuppertal, Germany. E-mail: dirklh@uni-wuppertal.de

The hard X-ray beamline BL8 at the superconducting asymmetric wiggler at the 1.5 GeV Dortmund Electron Accelerator DELTA is described. This beamline is dedicated to X-ray studies in the spectral range from  $\sim 1$  keV to  $\sim 25$  keV photon energy. The monochromator as well as the other optical components of the beamline are optimized accordingly. The endstation comprises a six-axis diffractometer that is capable of carrying heavy loads related to non-ambient sample environments such as, for example, ultrahigh-vacuum systems, high-pressure cells or liquid-helium cryostats. X-ray absorption spectra from several reference compounds illustrate the performance. Besides transmission measurements, fluorescence detection for dilute sample systems as well as surface-sensitive reflection-mode experiments have been performed. The results show that high-quality EXAFS data can be obtained in the quick-scanning EXAFS mode within a few seconds of acquisition time, enabling time-resolved *in situ* experiments using standard beamline equipment that is permanently available. The performance of the new beamline, especially in terms of the photon flux and energy resolution, is competitive with other insertion-device beamlines worldwide, and several sophisticated experiments including surface-sensitive EXAFS experiments are feasible.

© 2009 International Union of Crystallography  
Printed in Singapore – all rights reserved

**Keywords:** X-ray absorption spectroscopy; EXAFS; XANES; X-ray reflectivity; diffraction.

## 1. Introduction

The use of synchrotron radiation is important for many applications in materials science, especially for X-ray absorption spectroscopic experiments, where the energy dependence of the absorption coefficient is measured in the vicinity and above an absorption edge of the element of interest. Electron or positron storage rings together with insertion devices are essential for creating brilliant X-ray beams in a wide spectral range. Owing to the increasing demand for highly brilliant and intense hard X-rays, additional dedicated synchrotron radiation sources are under construction worldwide.

The new beamline is installed at the superconducting asymmetric wiggler in the DELTA storage ring of the University of Dortmund, Germany (Tolan *et al.*, 2003). The storage ring usually operates at an electron energy of 1.5 GeV, injection currents of 120 mA and about 8–10 h of lifetime. The beamline was designed for X-ray absorption spectroscopy, diffraction measurements and surface-sensitive X-ray reflectivity experiments in the energy range between  $\sim 1$  keV and 25 keV (12.4–0.49 Å), making use of the intense radiation

emitted by the superconducting wiggler. Accordingly, three different pairs of monochromator crystals, namely Si(311), Si(111) and YB<sub>66</sub>(400), are mounted in a complex triple monochromator. The beamline and its components were manufactured by ACCEL (Bergisch Gladbach, Germany). Up to now, there are only few beamlines that offer the technologically important spectral range between 1 and 2 keV using YB<sub>66</sub> crystals (see, for example, Rowen *et al.*, 1993; Kinoshita *et al.*, 1998; Wong *et al.*, 1999; Kitamura *et al.*, 2003; Akabayov *et al.*, 2005). Beamline X15B at the NSLS allows the use of several different monochromator crystals such as beryl, InSb and Si and covers the spectral range between  $\sim 0.8$  and 15 keV; however, it is required to break the vacuum of the monochromator vacuum chamber to interchange the available crystal pairs (MacDowell *et al.*, 1989). Since the DELTA beamline 8 allows the use of hard X-ray beams in addition to the soft X-rays from the YB<sub>66</sub>, very interesting and important fields of research can be addressed using complementary soft and hard X-rays on the same sample without a transfer to another instrument. This makes it possible to investigate different elements in a sample or the consecutive measurement of *K*- and *L*-edges of the same element, *e.g.* Br with the *K*-edge at 13.474 keV and the *L*-edges at 1.782, 1.596 and 1.550 keV,

‡ Present address: Helmholtz-Zentrum Potsdam, Deutsches GeoForschungs-Zentrum, Sektion 3.3, Telegrafenberg, D-14473 Potsdam, Germany.

**Table 1**

Specifications of the BL8 beamline and of the wiggler source.

DELTA storage ring current	Typically 120 mA injection current, 8–10 h lifetime	
BL8 source	Superconducting wiggler	
Front-end slits (m from source)	22.1	
Mirror 1 (M1) (m from source)	24.5, pitch $-5$ mrad up to $5$ mrad	
Monochromator (m from source)	27.7 [Si(311)], 28.3 [Si (111) and YB <sub>66</sub> ]	
Mirror 2 (M2) (m from source)	31.3, pitch $-5$ mrad up to $5$ mrad	
Mirror 3 (M3) (m from source)	38.1, pitch $-5$ mrad up to $25$ mrad	
Diffraction endstation (m from source)	39.1	
	Symmetric mode	Asymmetric mode
Magnetic field (T)	2.79	5.3
Magnetic period (cm)	14.4	28.8
Magnetic gap (mm)	18	18
Number of poles	20 (10 periods)	10 (5 periods)
Wiggler $K$ parameter	36	149
Radiation power (W mrad <sup>-2</sup> mA <sup>-1</sup> )	0.84	1.59
Critical energy, $E_c$ (keV)	4.18	7.93
Source flux at $E_c$ (calculated) [s <sup>-1</sup> mA <sup>-1</sup> mrad <sup>-1</sup> (0.1% bandwidth) <sup>-1</sup> ]	$3.4 \times 10^{11}$	$1.1 \times 10^{11}$
Source size ( $\mu\text{m}$ )	$80 \times 360$ (v $\times$ h)	$80 \times 360$ (v $\times$ h)
Source divergence (mrad)	$\pm 0.34 \times \pm 13$ (v $\times$ h)	$\pm 0.34 \times \pm 25$ (v $\times$ h)
Flux at sample (measured) (s <sup>-1</sup> mA <sup>-1</sup> mm <sup>-2</sup> )		$\sim 10^7$ [Si(111) at 9 keV, 0.017% bandwidth] $\sim 3 \times 10^6$ [Si(311) at 20 keV, 0.004% bandwidth]
Beam size at the sample (mm)		Typically $1 \times 10$ (v $\times$ h) Focused: $0.5 \times 0.5$ Slits: 0.05–25 (h), 0.05–2 (v)

respectively. Furthermore, the  $M$ -edges of heavy fermion systems such as those of mercury, bismuth or gold are accessible besides their  $L$ -edges.

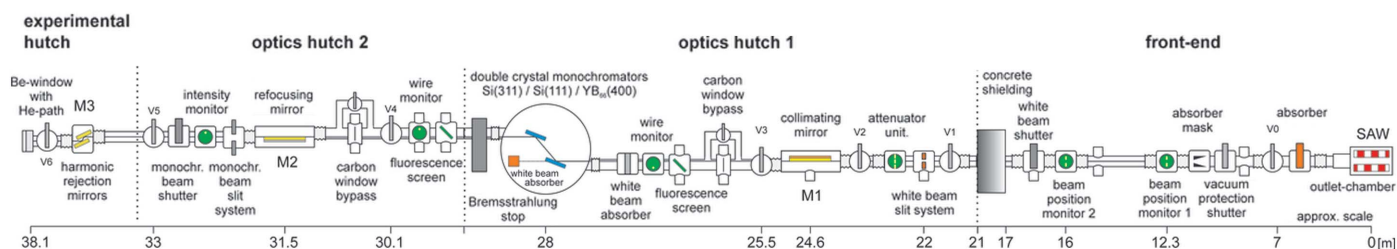
In the following, we describe the optical layout and the performance of the beamline including first measurements making use of the unique experimental possibilities provided there.

## 2. X-ray source and beamline

### 2.1. X-ray source and front-end layout

As mentioned above, the X-ray source is a liquid-helium-cooled superconducting wiggler with 20 poles with a magnetic gap of 18 mm that can be switched between two different operation modes. In the symmetric mode, ten periods of a magnetic field of 2.79 T result in a wiggler parameter  $K = 37$  and a radiation fan of  $\pm 13$  mrad horizontal beam divergence with a critical energy of 4.1 keV. The standard mode of

operation is, however, the asymmetric mode, where the magnetic field is increased to 5.3 T (wiggler parameter  $K = 149$ ), resulting in a reduced number of five periods. In this mode the horizontal beam divergence amounts to  $\pm 25$  mrad, and the critical energy to about 8 keV. This broad radiation fan is used by the three beamlines BL8 (which is described here), BL9 (Paulus *et al.*, 2005; Krywka *et al.*, 2006, 2007) and BL10. Each of those beamlines utilizes  $5 \text{ mrad} \times 0.7 \text{ mrad}$  (horizontal  $\times$  vertical) of the radiation as defined by a fixed water-cooled absorber mask  $\sim 12 \text{ m}$  from the centre of the source. While the surface diffractometer as well as the small-angle and wide-angle X-ray scattering set-ups of BL9 are installed in the horizontal centre of the wiggler fan, BL8 and BL10 are aligned  $\pm 15$  mrad to both sides, which gives extremely limited space for all the beamline instrumentation, especially in the front-end. The full specification of the wiggler and resulting properties of the beamline are summarized in Table 1. A schematic representation of the beamline layout is given in Fig. 1.


**Figure 1**

Schematic representation of the basic beamline concept of the DELTA beamline BL8. The first mirror M1 collimates the wiggler beam vertically to a double-crystal monochromator with three different pairs of monochromator crystals that can be exchanged by remote control. The second mirror M2 refocuses the beam onto the sample on the diffractometer endstation. The third mirror system M3 provides harmonic rejection for low-energy photon beams ( $E < 4$  keV). The transfer line between the second optics hutch and the experimental hutch is not shown in this figure.

The front-end of the beamline, consisting of the photon absorber, a fast vacuum protection shutter, the absorber mask and the white-beam shutter as well as two beam-position monitors at a distance of  $\sim 4$  m, is located inside the concrete shielding that surrounds the storage ring. The white-beam slit system equipped with water-cooled and motorized copper blades as well as an attenuator unit with four different filter foils (1 mm C, 3 mm C, 30  $\mu\text{m}$  Cu and 1.5 mm Al) for the reduction of the heat load on the X-ray optical components are located in the first optics hutch and complete the front-end section

### 2.2. Mirrors and monochromator

The first optics hutch contains the first downward-reflecting mirror M1 located at about 24.5 m from the source, which provides collimation in the vertical direction. It is also used for removal of higher-order harmonics from the beam. The mirror (manufactured by Crystal Scientific, Rennington, Alnwick, UK) consists of a silicon block with a 50 nm Rh coating (*L*-edges between 3.0 and 3.4 keV, *K*-edge at 23.2 keV) and has an optically active length of 1000 mm and a width of 60 mm. The optical surface exhibits a roughness of  $\sim 3$  Å. The heat load from the impinging radiation is 391 W  $\text{mrad}^{-2}$  at 15 mrad from the horizontal centre. This gives a maximum power of 195 W absorbed by the first mirror at its maximum glancing angle of 5 mrad. An indirect water-cooling system is mounted on both sides of the mirror. The cylindrical bending radius can be varied between 3500 m and a plane surface by means of a four-cylinder bender manufactured by SESO (Aix-en-Provence, France).

Downstream of the first mirror, the double-crystal monochromator is located at about 28 m distance from the source. The vacuum of the monochromator chamber is separated from that of the mirror by a thin (50  $\mu\text{m}$ ) carbon foil which also reduces the heat load on the monochromator. Owing to the large energy range covered by the beamline, three individual crystal pairs are mounted on two different goniometers as shown in Fig. 2. The angular range of both goniometers is from  $-3^\circ$  to  $+70^\circ$ . Monochromator optics 1 (27.7 m from the source) accommodates a pair of Si(311) crystals for the spectral range from about 8 keV to  $\sim 30$  keV, while optics 2 (28.3 m from the source) consists of a pair of Si(111) crystals (2.1–14 keV) and an additional pair of YB<sub>66</sub> crystals (Wong *et al.*, 1990, 1999; Rowen *et al.*, 1993). Both crystal pairs of optics 2 can be exchanged in the beam within a few minutes by means of a lateral translation perpendicular to the beam, a method first demonstrated at HASYLAB (Frahm, 1995). The surfaces of the first crystal of each of the crystal pairs are mounted in the centre of rotation of the respective goniometers. With a lattice spacing of 5.86 Å for the (400) lattice planes, the YB<sub>66</sub> crystals can be efficiently used for the soft X-ray range between 1.13 and 2.07 keV (see, for example, Wong *et al.*, 1995) covering the technologically important *K*-edges of Mg (1.303 keV), Al (1.559 keV) and Si (1.839 keV) and the *L*-edges of, for example, Ga (1.12–1.30 keV), Ge (1.22–1.42 keV) and As (1.32–1.53 keV). However, it should

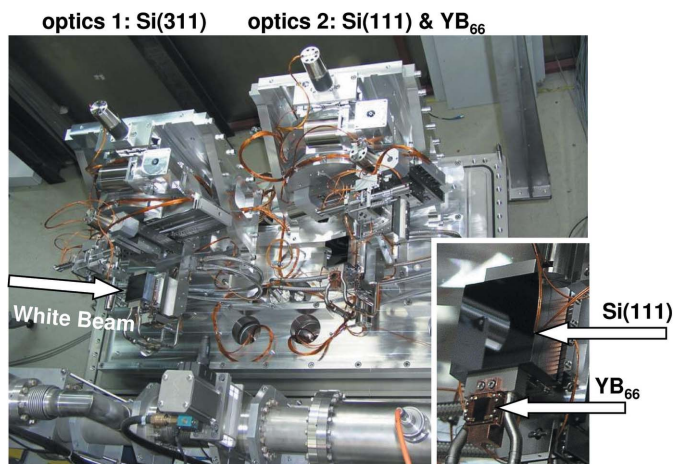


**Figure 2**

Photograph of the triple monochromator of the DELTA beamline. Two separate goniometers are installed, one for Si(111) and YB<sub>66</sub> (optics 2), the other for Si(311) crystal pairs (optics 1). In the inset the U-shaped first Si(111) crystal as well as the significantly smaller YB<sub>66</sub> crystal are displayed. At the bottom of the figure the flight tube of BL9 (15 mrad horizontal offset) can be seen, illustrating the limited space between the different beamlines using the radiation from the superconducting asymmetric wiggler.

be mentioned that successful test experiments using the YB<sub>66</sub> monochromator crystals have been performed at energies around the Ti *K*-edge at 5 keV, which shows that there is no energy gap at the beamline between the different crystals available, although the energy resolution of the YB<sub>66</sub> is decreasing at those higher energies. Both goniometers can be adjusted vertically by about 50 mm to the variable first mirror pitch. All the first crystals are indirectly water cooled, with the cooling being designed for heat loads of up to 500 W. For the Si(111) and the Si(311) crystals, the cooling is combined with a bending mechanism to compensate for the thermal bump induced by the high heat load of the wiggler (Zaeper *et al.*, 2002). For this purpose the legs of the U-shaped crystals [80 mm  $\times$  80 mm (length  $\times$  width) of the reflecting Si surfaces] can be spread by a metal bellow actuated by compressed air, thereby increasing the Bragg-reflected intensities and narrowing the corresponding rocking curves (Zaeper *et al.*, 2002; Dudzik *et al.*, 2006). This way, the crystal surfaces can be compensated over a length of about 50 mm. While the second Si(111) crystal is a planar crystal, the second Si(311) crystal is mounted in an ESRF-type sagittal bender (Freund *et al.*, 1998) with a variable bending radius between 1 m and  $\sim 160$  m. The second crystals can be translated vertically by 50 mm and along the beam direction by 200 mm, allowing a fixed-exit beam geometry for all crystal pairs. Additional degrees of freedom allow stepper-motor-controlled adjustments of the crystals in yaw, roll and pitch. The pitch can further be fine-tuned using piezo-electric actuators, which are routinely used for the detuning of the monochromator crystals pairs with respect to each other to remove higher-order harmonics as well as for the stabilization of the monochromator intensity during, for example, EXAFS scans by means of a digital monochromator stabilization unit

(SIS2900 D-Mostab; Meß *et al.*, 1998). By controlled detuning of the monochromator crystals from parallel alignment, the transmitted intensity can be adjusted to a specified fraction of the maximum flux in the rocking curve as described by Krolzig *et al.* (1984). Angular encoders are installed at both goniometers for precise Bragg-angle readouts. After proper alignment, rocking-curve measurements with an ionization chamber show that the full widths at half-maximum,  $\Theta_{\text{FWHM}}$ , are close to the values predicted by the Darwin theory for Si(111) and Si(311). In the case of Si(111) the measured rocking-curve width value is  $\Theta_{\text{FWHM}} = 11.94 \pm 0.19$  arcsec for a photon energy of  $E = 7$  keV and for Si(311) at  $E = 14$  keV this value is  $\Theta_{\text{FWHM}} = 2.42 \pm 0.01$  arcsec, in comparison with the calculated widths of 11.72 and 2.18 arcsec, respectively.

The YB<sub>66</sub> crystals are significantly smaller in size ( $\sim 15$  mm length and 20 mm width, 1 mm thickness), and no bending mechanisms can be used here. The carbon filter foils in the front-end are strongly absorbing at lower photon energies and cannot be used in the low energy range. Thus the filter system offers an additional relatively small aperture (15 mm  $\times$  4 mm), which acts as a differential pumping stage. The X-ray beam can pass unrestricted without any absorption, and the cross section of this bypass is small enough to maintain the required vacuum conditions in the monochromator and the mirror sections. A second similar C-filter/differential bypass system is placed in front of the second, upward-reflecting, mirror M2 located at about 31.3 m from the source. This focusing mirror with an active length of 1000 mm and a width of 60 mm is mounted on a second bender (manufactured by SESO) and has a variable bending radius between 2.2 km and infinity. Its sagittal cylindrical curvature of 47 mm is optimized for a glancing angle of 3.5 mrad = 0.20°. Together with the Rh-coating of the mirrors, this corresponds to a critical energy of about 17 keV. A third mirror system M3 is installed in the experimental hutch 38.2 m from the source. It is constructed similar to that of Saintavit *et al.* (1989) and was designed to meet the requirements for harmonic rejection at low energies in the range below  $\sim 4$  keV. It consists of three pairs of glass stripes each of length 200 mm and optical width 80 mm. While one of the mirror pairs is made of uncoated Pyrex glass, the two other pairs are coated with 50 nm of Cr and Rh. Making use of grazing angles of up to 25 mrad ( $\sim 1.43^\circ$ ), the critical angle of this mirror assembly can be adjusted down to 2.0 keV, so that an effective harmonic rejection is possible also for the spectral range of the YB<sub>66</sub> monochromator. The performance of this mirror device and the YB<sub>66</sub> monochromator will be described in a separate publication.

### 2.3. Beam-position and intensity monitors

Along the beamline, several detectors and fluorescence screens are installed. Two beam-position monitors are included in the front-end section. The first fluorescence screen is installed at a distance of about 25.7 m from the wiggler source for the characterization of the direct beam and the mirrored pink beam reflected downwards by mirror M1. A wire monitor as well as a calorimeter are installed here in

addition. A second fluorescence screen is installed at 29.6 m from the source for the inspection of the monochromated beam downstream of the double-crystal monochromator. A further wire monitor is located  $\sim 30$  m from the source. Downstream of mirror M2, a further intensity monitor at 32.5 m for the inspection of the refocused beam completes the permanently available beam-monitoring equipment. Here, X-rays scattered from a Kapton foil of thickness 75  $\mu\text{m}$  at an angle of 45° towards the beam are detected by a 100 mm<sup>2</sup> Si photodiode to obtain a reference intensity signal. The slit system downstream of the monochromator and the mirror M2, located in the optics hutch 2, and the sample slit system are used to define the size of the beam on the sample. During typical EXAFS scans covering more than 1 keV, no detectable beam position variations are visible, making, for example, grazing-incidence EXAFS experiments as described in §4.3 feasible, where the vertical beam size is typically in the range 50  $\mu\text{m}$  to  $\sim 250$   $\mu\text{m}$ .

## 3. Experimental station

### 3.1. Experimental hutch

The experimental hutch of BL8 at DELTA is located downstream of that of beamline BL9, and thus a lead-shielded UHV transfer line of diameter 100 mm stretches between the second optics hutch and the experimental hutch. A large-area Be window (700  $\mu\text{m}$  thickness, 70 mm height, 40 mm width) protects the ultrahigh vacuum of the beamline at the exit flange in the experimental hutch. A manually operated UHV valve with a special venting option is mounted between the mirror chamber M3 and the Be window, and thus this window can be exchanged or removed without venting the vacuum system. Furthermore, fully evacuated sample stages for investigations at lower energies can directly be flanged to the beamline. In the standard operation mode a He-filled beam path is attached to the high-pressure side of the Be window (see Fig. 1) in order to minimize parasitic absorption in air for experiments at energies below  $\sim 7$  keV and to prevent oxidation or corrosion of the window.

The experimental hutch with an area of length 3.4 m, width 3.3 m and a height of  $\sim 2.8$  m accommodates the mirror system M3 as well as the large user diffractometer (see §3.2). Ionization chambers with different lengths (15 cm and 30 cm) and different gases (He, N<sub>2</sub>, Ar and Kr) are available at the beamline as intensity monitors for diffraction, reflectivity and EXAFS experiments. Furthermore, a NaI scintillation counter as well as large area Si pin diodes are available with current amplifiers and counter electronics. In addition, a Peltier-cooled Si PIN-diode and a Si drift diode with pulse digital processing electronics (Amptek Inc., Bedford, USA) are permanently available for X-ray fluorescence and X-ray standing wave (XSW) experiments (see, for example, Zegenhagen, 1993). First results of XSW experiments at BL8 have just been achieved and will be published elsewhere.

While a thinner Be window (200  $\mu\text{m}$ ) is available for intermediate X-ray energies at around 4–5 keV, a new high-

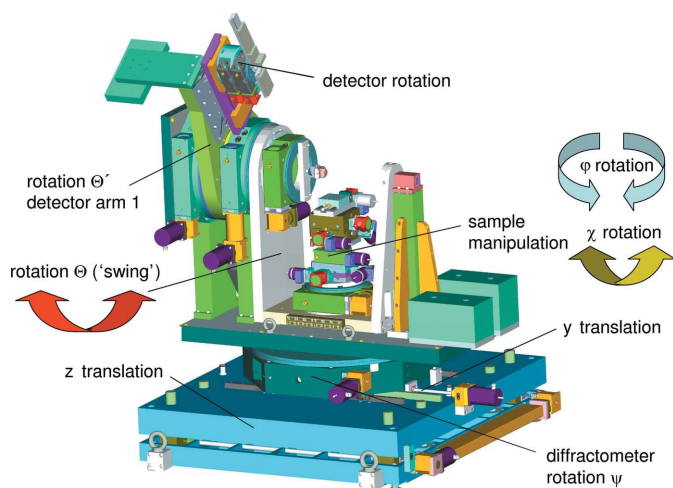


**Figure 3**  
Schematic representation of the multi-purpose diffractometer installed at the DELTA materials science beamline. The most important rotation circles are indicated.

vacuum sample stage for XAFS measurements with the YB<sub>66</sub> optics is under construction. It will be directly connected to the beamline vacuum by replacing the Be windows, thus allowing windowless operation. Electron and fluorescence-yield X-ray measurements are planned.

### 3.2. Diffractometer

The multi-purpose six-circle user-diffractometer endstation is installed at ~39 m from the source. A schematic representation as well as the most important rotation circles are given in Fig. 3. The diffractometer offers a high load base for adjustments to different vertical beam positions. The unique feature of this diffractometer is a large swing-like sample stage of width 54 cm perpendicular to the beam and 40 cm in the beam direction that can accommodate heavy sample environments of up to ~200 kg. These set-ups are required for many *in situ* studies using, for example, ultrahigh-vacuum systems, low-temperature cryostats or bulky large-volume high-pressure cells like the Paris–Edinburg cell (Besson *et al.*, 1992), for example. The swing has an angular range of ±15°, so that conventional X-ray diffraction studies in several geometries as well as grazing-incidence X-ray reflectivity experiments are feasible in direct combination with all kinds of X-ray absorption experiments. Some of the sample manipulators (translations/rotations) inside the huge swing may be removed for specific experiments. First successful X-ray diffraction experiments on CdSe colloids and nanoparticles, as well as specular X-ray reflectivity and grazing-incidence diffraction measurements on thin films, have already demonstrated the possibility of such experiments at DELTA.

### 3.3. Beamline control system

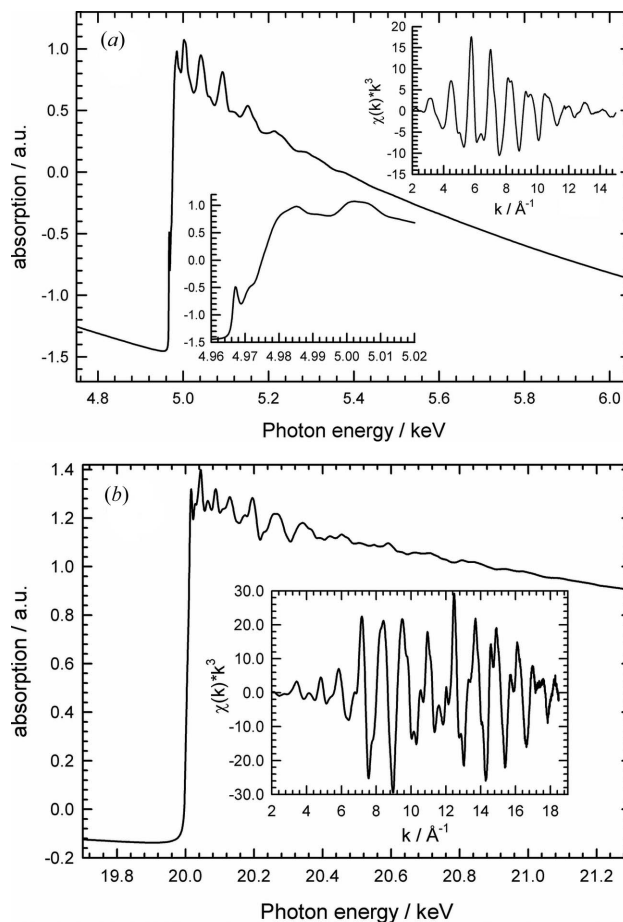
The control of all stepper motors as well as the experimental data collection is performed by a control software based on the package *SPEC* (Certified Scientific Software, <http://www.certif.com/>). *SPEC* communicates with the

different motors, detectors and devices *via* different communication hardware and protocols such as VME, GPIB, RS232, USB and TCP/IP. The user interface for beamline, diffractometer and detector equipment allows specialized online data analysis routines as well as macros for a variety of scans for diffraction, reflectivity and energy, *i.e.* EXAFS scans. Implemented are digital pulse processing and analysis of photon-counting systems like fluorescence detectors including the definition of regions of interest for fluorescence EXAFS experiments (see below).

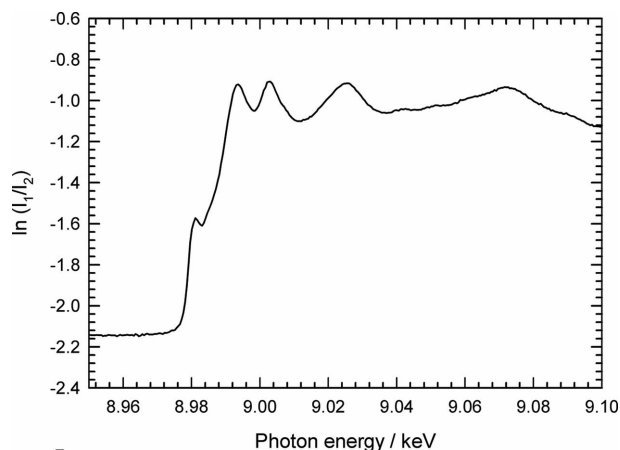
## 4. XAFS experiments

### 4.1. Transmission-mode XAFS experiments

During the commissioning of the beamline, several metal foils have been measured as references. Fig. 4(*a*) shows data from a Ti metal foil using N<sub>2</sub>-filled ionization chambers and Si(111) monochromator crystals, while Si(311) and Ar-filled ionization chambers were used for the Mo metal transmission spectrum shown in Fig. 4(*b*). The obtained data quality is generally excellent with respect to the reproduction of sharp



**Figure 4**  
Room-temperature transmission-mode spectra of metal foils: (*a*) 5 μm Ti metal foil at the Ti *K*-edge measured using the Si(111) monochromator. The insets show the XANES region and the *k*<sup>3</sup>-weighted EXAFS. (*b*) 20 μm Mo metal foil at the Mo *K*-edge. The inset shows the extracted *k*<sup>3</sup>-weighted EXAFS.


**Figure 5**

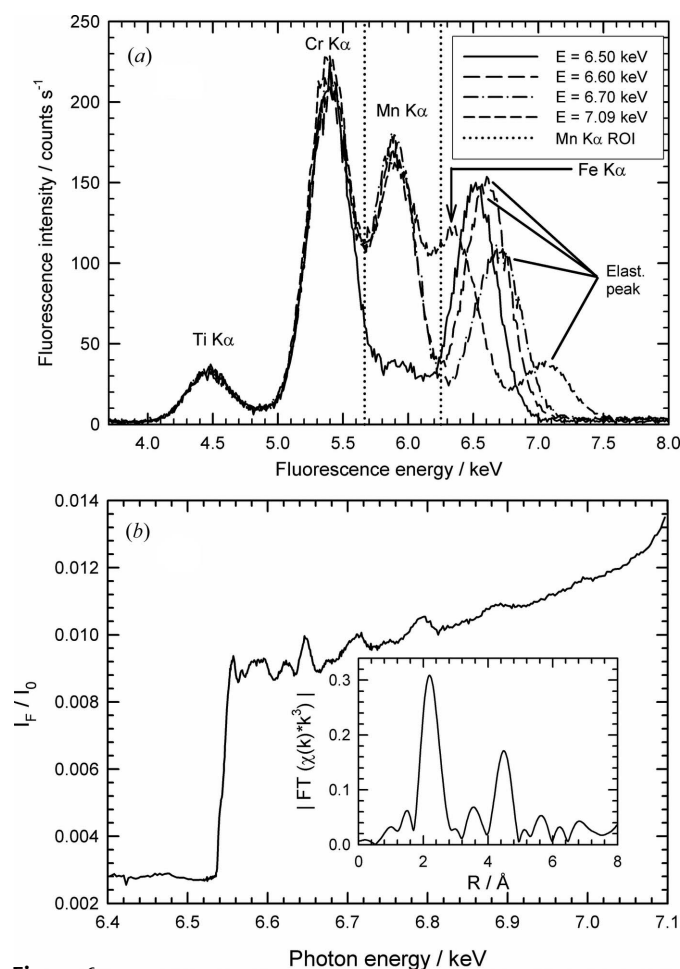
Transmission-mode XANES at the Cu  $K$ -edge of a Cu metal foil in the quick-EXAFS mode, measured within  $\sim 18$  s. The distinct Cu metal pre-edge peak at about 8981.5 eV shows the excellent energy resolution of the monochromator.

absorption features close to edges as well as to the low noise of the  $k^3$ -weighted  $\chi(k)$  data, up to wavenumbers close to even  $20 \text{ \AA}^{-1}$  as in the case of the Mo foil spectrum. Thus the beamline can be used for high-resolution XANES spectroscopy as well as for the application of the extended X-ray absorption spectroscopy technique in the spectral range between approximately 4 keV and 25 keV. Besides conventional step scan mode data collection, the so-called quick-scanning EXAFS (QEXAFS) method is possible, in which overheads associated with all movements of a monochromator using a point by point scheme are eliminated by scanning the spectrum continuously. Thus spectra measured on the fly are possible within a few seconds (Frahm, 1989). In Fig. 5, a typical QEXAFS spectrum measured in transmission on a Cu metal foil is presented. The data were taken within 18 s with an energy resolution of about 1.12 eV including core hole lifetime effects, which is close to the natural width of the Si(111) rocking curve. This is obvious from the pre-edge peak at the Cu metal  $K$ -edge. It should be noted that the stability of the energy calibration is excellent: the offset between subsequent scans was found to be less than 0.1 eV, which makes precise XANES experiments feasible. Variations of less than 0.5 eV were found for the long time stability of the monochromator within a week of operation at different absorption edges and making use of the remote crystal exchange function.

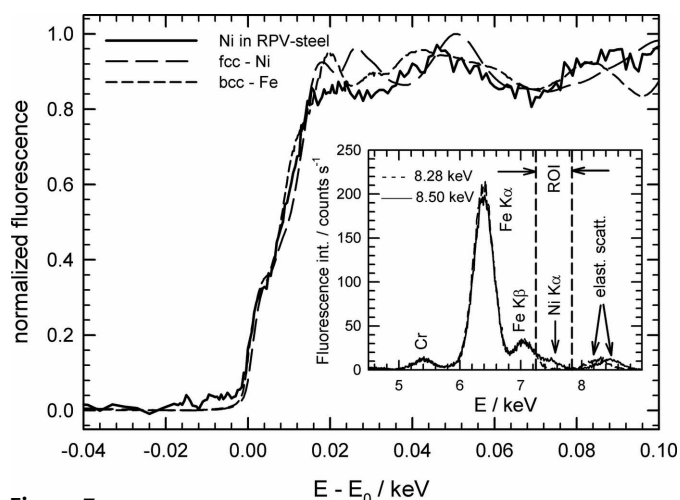
#### 4.2. Fluorescence-mode XAFS experiments

Fluorescence-mode XAFS experiments are important for samples that cannot be penetrated by X-rays and samples where the element of interest is present in a low concentration only. We performed several fluorescence XAFS experiments on Fe base-steels containing alloyed metal species in low amounts. The alloyed elements in steels are important for, for example, the elastic properties of materials. Small precipitates of the alloyed elements of a few nanometres in size that are formed during alloy fabrication may pin dislocations and hinder dislocation gliding, thus leading to a less ductile behaviour compared with a homogeneous dispersion in the

steel matrix. The local structure and the position of the alloyed elements in the Fe host matrix are important to couple the microstructural information with the mechanical behaviour of such steels. In Fig. 6, fluorescence spectra of an Fe base-steel (RPV steel) containing  $\sim 1$  at% Mn are shown for excitation energies in the vicinity of the Mn  $K$ -edge at 6.539 keV. Besides the Mn and Fe signals (only for the highest excitation energy of 7.09 keV, which is slightly below the Fe  $K$ -edge at 7.112 keV), X-ray fluorescence peaks of Ti and Cr are detectable in similar amounts as Mn. Using the Mn fluorescence photons in the energy range between 5.66 keV and 6.25 keV, the EXAFS spectrum in Fig. 6(b) was obtained. Despite the low Mn concentration within the alloy and a total integration time of only 1 h for the energy range 6.4–7.1 keV, the quality of the spectrum allows a more detailed and quantitative EXAFS analysis. The increase of the fluorescence yield at energies above  $\sim 6.7$  keV is related to the onset of the Fe  $K\alpha$  excitation in the pre-edge region of the Fe host lattice, which prevents the complete discrimination of the Mn and Fe contributions. The Fourier transform (FT) of the  $k^3$ -weighted


**Figure 6**

(a) Fluorescence spectra of an Fe alloy containing 1 at% Mn for different excitation energies in the vicinity of the Mn  $K$ -edge (6.539 eV) as indicated. (b) Raw fluorescence EXAFS at the Mn  $K$ -edge of the Fe base alloy within  $\sim 1$  h of total integration time. The data are extracted from the data of (a) using the region of interest (ROI) indicated by the vertical dotted lines. The inset shows the magnitude of the Fourier transform of the  $k^3$ -weighted EXAFS fine structure.


**Figure 7**

Normalized fluorescence Ni *K*-edge XANES spectrum of an iron sample alloyed with ~1 at% of Ni (RPV steel). The spectrum is calibrated relative to the Ni *K*-edge at 8.333 keV. For comparison, the XANES *K*-edge spectra (measured in transmission) of Ni (f.c.c. structure) and Fe (b.c.c.) foils are shown. The inset shows the fluorescence spectra obtained from the alloy sample for two different excitation energies. The Ni XANES data were determined using the indicated region of interest (ROI).

Mn EXAFS is shown in the inset of Fig. 6(b). The alloyed Mn atoms are located on regular body-centred-cubic (b.c.c.) sites, which can be seen by a comparison with a b.c.c. metal such as pure iron or alloyed elements in b.c.c. iron positions (Edwards *et al.*, 1999).

The situation is more complicated in the case of an iron sample alloyed with nickel as can be seen in the inset of Fig. 7. First of all, the single-element Si detector is exposed to a significantly higher photon flux compared with the experiments at the Mn *K*-edge, since the iron *K*-fluorescence of the Fe host is also excited at the Ni *K*-edge. Thus the photon statistics for the Ni fluorescence radiation is worse in comparison with the Mn edge data. Besides intense Fe *K* $\alpha$  and *K* $\beta$  peaks at ~6.4 keV and 7.1 keV, Cr fluorescence is visible at ~5.4 keV. A small Ni peak can be identified at the high-energy side of the intense Fe *K* $\beta$  peak. Those Ni contributions were determined from the fluorescence spectra between 7.25 keV and 7.84 keV, resulting in the near-edge X-ray absorption spectrum shown in Fig. 7. The XANES data were obtained within about 30 min of integration time. Considering the strong overlap of the intense Fe signals with the weak Ni signals, the spectrum is of significant quality. The comparison with a face-centred-cubic (f.c.c.) Ni metal foil and a b.c.c. Fe metal foil clearly shows that the XANES resembles the b.c.c. structure of iron, suggesting again that the alloyed atoms reside on b.c.c. lattice sites. These findings are in good agreement with previous studies of Fe materials weakly alloyed with Cu and Ni (Edwards *et al.*, 1999).

#### 4.3. Reflection-mode XAFS experiments

Grazing-incidence X-ray absorption spectroscopy is an excellent method for studying the near-surface structure of thin films, surfaces, adsorbates *etc.* (see, for example, Heald *et*

*al.*, 1988; Borthen & Strehblow, 1995; d'Acapito *et al.*, 2000; Lützenkirchen-Hecht *et al.*, 2003). Here we investigate the *in situ* growth of thin films on a substrate at cryogenic temperatures well below 40 K. In this temperature range, film properties and growth modes can be completely different from those at elevated temperatures. Thus, film growth at low temperatures is a research field of fundamental interest (see, for example, Danilov *et al.*, 1995; Ekinici & Valles, 1999; Long & Valles, 2005). Many investigations claim the presence of strongly disordered or even amorphous phases for films deposited at low cryogenic temperatures. However, a direct structural investigation using XAFS is essential to manifest those conclusions. Here we present the first results obtained *in situ* during the growth of thin Bi films on smooth float glass substrates for deposition temperatures around 15 K. The experiments were performed using an ultrahigh-vacuum sample preparation system with turbomolecular pump, evaporation units, mass spectrometer and equipment for electrical resistivity measurements. In parallel, X-ray experiments could be performed *in situ*. Only the most important features of the set-up are described here, and additional information will be given in a detailed publication (Markert *et al.*, 2009). The system, based on a liquid-helium cryostat with cryogenically cooled heat shields and differentially pumped Kapton X-ray windows, is able to maintain a vacuum of  $10^{-9}$  mbar, ensuring clean vacuum conditions even for prolonged experiments. It weighs about 100 kg, and the unique capabilities of the diffractometer installed at the DELTA beamline are required allowing proper alignment and movements of each sample in the beam. In Fig. 8 the specular X-ray reflectivity for fixed photon energies are presented directly after the deposition of an 18 nm thin Bi metal film as well as after its annealing to 300 K. Only smaller changes of the reflectivity profiles are detectable. More specifically, the amplitudes of the Kiessig fringes at higher incidence angles  $\varphi > 0.5^\circ$  are reduced for the annealed film, indicating that the surface roughness of the film increases during the annealing process. Reflection-mode EXAFS were measured for an incidence angle  $\varphi = 0.242^\circ$ . The data in the inset of Fig. 8 prove the increased roughness of the annealed film by the overall reduction in reflectivity. Furthermore, the amplitudes of the EXAFS fine-structure oscillations above the Bi *L*<sub>3</sub>-edge are also reduced in amplitude. A straightforward discussion of these features is, however, not straightforward because of changes of both the static and dynamic disorder in the Bi thin films during annealing. However, those are first indications for structural changes since the amplitude of the EXAFS remains reduced after cooling of the Bi films back to their deposition temperature (Markert, 2009).

#### 5. Conclusions

The materials science X-ray beamline BL8 at the DELTA storage ring provides a stable high-flux X-ray beam for a wide range of investigations and different non-ambient (vacuum, gas- and liquid-phase, cryogenic and high-temperature) environments. Besides conventional transmission and fluor-

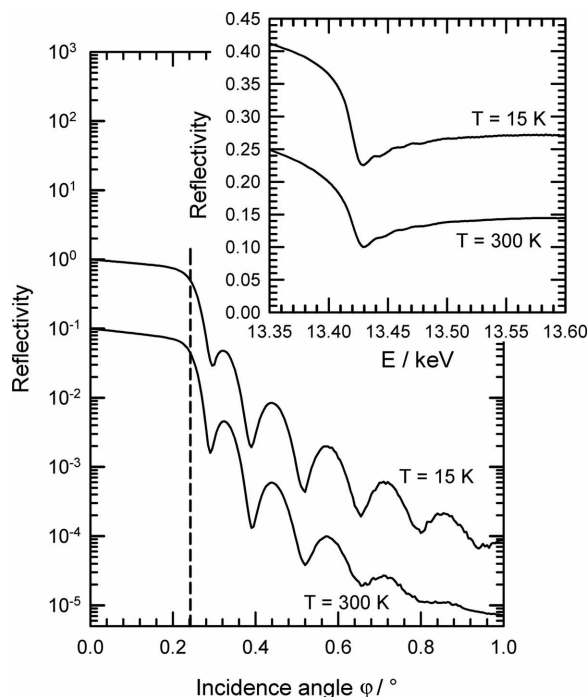


**Figure 8**

*In situ* measured specular reflectivity profiles (13.35 keV photon energy) of a thin Bi film (18 nm thickness) on a glass substrate, deposited and measured at 15 K, and after annealing at 300 K. Reflection-mode EXAFS spectra at the Bi  $L_3$ -edge (13.419 keV) were measured for  $\varphi = 0.242^\circ$  (dashed vertical line) and are depicted in the inset. The strong reduction of the overall reflectivity as well as the smaller EXAFS oscillations are obvious after warming up the films to 300 K.

escence detection modes, grazing-incidence X-ray absorption spectroscopy as well as X-ray reflectivity and X-ray diffraction experiments are feasible making use of the robust multi-purpose diffractometer. The two different pairs of monochromator crystals [Si(111) and Si(311)] for the photon energy range between  $\sim 2.1$  keV and 30 keV cover most of the technologically important X-ray absorption edges. Making use of these opportunities, the beamline has been in user operation since spring 2008, and first experiments including transmission-, fluorescence- and reflection-mode XAFS studies, XSW and X-ray diffraction investigations have already been performed. After commissioning of the YB<sub>66</sub> crystals for the energy range between 1.1 keV and 2.1 keV in the near future, X-ray absorption, scattering and diffraction experiments between 1 keV and 30 keV will be possible. The first experiments using YB<sub>66</sub> showed that there is a substantial overlap in the energy range between YB<sub>66</sub> and Si(111) optics. Therefore detailed investigation of different edges of both light and heavy constituent elements in the sample are enabled, this way gaining a very detailed view of the atomic and electronic structure of complex materials. The flexible optics allows focusing of the beam, so that small samples can be investigated with high flux, and grazing-incidence experiments such as X-ray reflectivity, diffraction and XAFS studies under *in situ* conditions are feasible. Making use of the versatile diffractometer, EXAFS experiments can be easily linked to diffraction or reflectometry. With the high stability and excellent

energy resolution of the monochromator in combination with the high photon flux offered by the wiggler source, time-resolved EXAFS experiments under *in situ* conditions are practicable, allowing real-time investigations of, for example, chemical reactions, catalysts or thin-film growth under *in situ* conditions.

This work was financially supported by the BMBF and the MWF NRW. Most parts of the beamline were manufactured and installed by ACCEL instruments (Bergisch Gladbach, Germany). The authors would like to thank the DELTA machine group for reliably providing synchrotron radiation and for manifold technical support during the installation and the commissioning phase of the beamline. The steel samples for the fluorescence XAFS experiments presented here were provided by S. Cammelli (Universität Wuppertal and PSI, Villigen, Switzerland). We further acknowledge the help of C. Markert with the cryocondensed thin-film preparation and data acquisition, and Alexej Herdt for his support during the commissioning of the YB<sub>66</sub> crystals.

## References

- d'Acapito, F., Mobilio, S., Cikmas, P., Merlo, V. & Davoli, I. (2000). *Surf. Sci.* **468**, 77–84.
- Akabayov, B., Doonan, C. J., Pickering, I. J., George, G. N. & Sagi, I. (2005). *J. Synchrotron Rad.* **12**, 392–401.
- Besson, J. M., Nelmes, R. J., Hamel, G., Loveday, J. S., Weill, G. & Hull, S. (1992). *Physica B*, **180–181**, 907–910.
- Borthen, P. & Strehblow, H.-H. (1995). *Phys. Rev. B*, **52**, 3017–3019.
- Danilov, A. V., Kubatkin, S. E., Landau, I. L., Parshin, I. A. & Rinderer, L. (1995). *Phys. Rev. B*, **51**, 5514–5517.
- Dudzik, E., Feyerherm, R., Diete, W., Signorato, R. & Zilkens, C. (2006). *J. Synchrotron Rad.* **13**, 421–425.
- Edwards, A. B., Roberts, K. J., Pizzini, S. & Phythian, W. J. (1999). *Philos. Mag. A*, **79**, 1295–1319.
- Ekinci, K. L. & Valles, J. M. Jr (1999). *Phys. Rev. Lett.* **82**, 1518–1521.
- Frahm, R. (1989). *Rev. Sci. Instrum.* **60**, 2515–2520.
- Frahm, R. (1995). HASYLAB Annual Report, pp. 113–114. DESY, Hamburg, Germany.
- Freund, A. K., Comin, F., Hazemann, J.-L., Hustache, R., Jenninger, B., Lieb, K. & Pierre, M. (1998). *Proc. SPIE*, **3448**, 144–155.
- Heald, S. M., Chen, H. & Tranquada, J. M. (1988). *Phys. Rev. B*, **38**, 1016–1026.
- Kinoshita, T., Takata, Y., Matsukawa, T., Aritani, H., Matsuo, S., Yamamoto, T., Takahashi, M., Yoshida, H., Yoshida, T., Ufuktepe, Y., Nath, K. G., Kimura, S. & Kitajima, Y. (1998). *J. Synchrotron Rad.* **5**, 726–728.
- Kitamura, M., Yoshikawa, H., Tanaka, T., Mochizuki, T., Vlaicu, A. M., Nisawa, A., Yagi, N., Okui, M., Kimura, M. & Fukushima, S. (2003). *J. Synchrotron Rad.* **10**, 310–312.
- Krolzig, A., Materlik, G., Swars, M. & Zegenhagen, J. (1984). *Nucl. Instrum. Methods Phys. Res.* **219**, 430–434.
- Krywka, C., Paulus, M., Sternemann, C., Volmer, M., Remhof, A., Nowak, G., Nefedov, A., Pöter, B., Spiegel, M. & Tolan, M. (2006). *J. Synchrotron Rad.* **13**, 8–13.
- Krywka, C., Sternemann, C., Paulus, M., Javid, N., Winter, R., Al-Sawalmih, A., Yi, S., Raabe, D. & Tolan, M. (2007). *J. Synchrotron Rad.* **14**, 244–251.
- Long, Z. & Valles, J. M. Jr (2005). *J. Low. Temp. Phys.* **139**, 429–438.
- Lützenkirchen-Hecht, D., Wagemaker, M., Keil, P., van Well, A. A. & Frahm, R. (2003). *Surf. Sci.* **538**, 10–22.
- MacDowell, A. A., Hasizume, T. & Citrin, P. H. (1989). *Rev. Sci. Instrum.* **60**, 1901–1904.

- Markert, C. (2009). PhD dissertation. Universität Wuppertal, Germany. (In German.)
- Markert, C., Lützenkirchen-Hecht, D., Wagner, R. & Frahm, R. (2009). *Europhys. Lett.* Submitted.
- Meß, K. H., Tröger, L. & Brüggmann, U. (1998). HASYLAB Annual Report, p. 42. DESY, Hamburg, Germany.
- Paulus, M., Fendt, R., Sternemann, C., Gutt, C., Hövel, H., Volmer, M., Tolan, M. & Wille, K. (2005). *J. Synchrotron Rad.* **12**, 246–250.
- Rowen, M., Rek, Z., Wong, J., Tanaka, T., George, G. N., Pickering, I. J., Via, G. H. & Brown, G. E. Jr (1993). *Synchrotron Radiat. News*, **6**, 25–28.
- Saintavit, P., Petiau, J., Manceau, A., Rivallant, R., Belakhovsky, M. & Renaud, G. (1989). *Rev. Sci. Instrum.* **60**, 2027–2029.
- Tolan, M., Weis, T., Wille, K. & Westphal, C. (2003). *Synchrotron Radiat. News*, **16**, 9–11.
- Wong, J., Rek, Z. U., Rowen, M., Tanaka, T., Schäfers, F., Müller, B., George, G. N., Pickering, I. J., Via, G., DeVries, B., Brown, G. E. Jr & Fröba, M. (1995). *Physica B*, **208–209**, 220–222.
- Wong, J., Shimkaveg, G., Goldstein, W., Eckart, M., Tanaka, T., Rek, Z. U. & Tompkins, H. (1990). *Nucl. Instrum. Methods Phys. Res. A*, **291**, 243–249.
- Wong, J., Tanaka, T., Rowen, M., Schäfers, F., Müller, B. R. & Rek, Z. U. (1999). *J. Synchrotron Rad.* **6**, 1086–1095.
- Zaeper, R., Richwin, M., Lützenkirchen-Hecht, D. & Frahm, R. (2002). *Rev. Sci. Instrum.* **73**, 1564–1567.
- Zegenhagen, J. (1993). *Surf. Sci. Rep.* **18**, 199–271.